

Hard thermal loop benchmark for the extraction of the nonperturbative $Q\bar{Q}$ potential

Yannis Burnier and Alexander Rothkopf

Institute for Theoretical Physics, Albert Einstein Center, University of Bern, Sidlerstrasse 5, CH-3012 Bern, Switzerland

(Received 1 May 2013; published 24 June 2013)

The extraction of the finite temperature heavy quark potential from lattice QCD relies on a spectral analysis of the Wilson loop. General arguments tell us that the lowest lying spectral peak encodes, through its position and shape, the real and imaginary parts of this complex potential. Here we benchmark this extraction strategy using leading order hard-thermal loop (HTL) calculations. In other words, we analytically calculate the Wilson loop and determine the corresponding spectrum. By fitting its lowest lying peak we obtain the real and imaginary parts and confirm that the knowledge of the lowest peak alone is sufficient for obtaining the potential. Access to the full spectrum allows an investigation of spectral features that do not contribute to the potential but can pose a challenge to numerical attempts of an analytic continuation from imaginary time data. Differences in these contributions between the Wilson loop and gauge fixed Wilson line correlators are discussed. To better understand the difficulties in a numerical extraction we deploy the maximum entropy method with extended search space to HTL correlators in Euclidean time and observe how well the known spectral function and values for the real and imaginary parts are reproduced. Possible venues for improvement of the extraction strategy are discussed.

DOI: [10.1103/PhysRevD.87.114019](https://doi.org/10.1103/PhysRevD.87.114019)

PACS numbers: 14.40.Pq, 03.65.Ge, 12.38.Gc, 12.38.Mh

I. INTRODUCTION

Twenty-seven years ago Matsui and Satz [1] proposed the melting of J/Ψ , i.e. the ground state of the $c\bar{c}$ vector channel, as a signal for the deconfinement transition in heavy-ion collisions. The recent success of relativistic heavy-ion experiments [2–5] in observing the relative suppression of charmonium and bottomonium serves as further motivation to develop a first principle description of the phenomena.

In the framework of effective field theories, heavy quarks can be described by nonrelativistic quantum chromodynamics (NRQCD) obtained from QCD by integrating out the hard energy scale, given by the rest mass of the heavy quarks. To describe the bound state of two quarks, one can further integrate out the typical momentum exchange between the bound quarks (see [6] and references therein), which leads to potential nonrelativistic QCD (pNRQCD). In this effective field theory the bound state is described by a two-point function satisfying a Schrödinger equation.

At zero temperature, the potential between a heavy quark and an antiquark is defined from the late time behavior of a Wilson loop and can be directly calculated in Euclidean-time lattice simulations or in perturbation theory. At small distances, where perturbation theory converges, both results agree [7].

At high temperatures, above the QCD phase transition, one might first expect that the problem becomes simpler, as the potential is not confining anymore. Actually, this is not the case since even a proper definition of the potential becomes nontrivial. In fact, the presence of a heat bath is most conveniently incorporated in a Euclidean space-time framework with compact temporal axis. There, the Wilson loop depends on imaginary time and needs to be

analytically continued to real time. Only from the large real-time, i.e. $t \rightarrow \infty$ behavior, can the finite temperature potential be extracted, and it happens to be complex [8,9] (for a QED scenario see e.g. [10]). Its imaginary part can be interpreted as Landau damping [11] and describes the decaying correlation of the $Q\bar{Q}$ system with its initial state due to scatterings in the plasma.

Along the lines presented in [8], one can compute the potential in finite temperature perturbation theory. This is a demanding task, as resummations need to be carried out in order to cure infrared divergences. To this day the full result is known only to leading order, whereas a short distance expansion has been calculated to higher order [12,13]. Even if higher orders were available, observing the deconfining transition will remain beyond the reach of perturbation theory.

In Ref. [14], a method was proposed to compute the heavy quark potential nonperturbatively from lattice QCD simulations. Starting from the measurement of the Euclidean Wilson loop on the lattice, its spectral function is reconstructed via the maximum entropy method (MEM). The definition of the potential is based on the peak structure of the Wilson loop spectrum.

Previous numerical evaluations, however, lead to unexpected results: both the real and imaginary parts appear to grow linearly at distances where other quantities, such as the free energies, already show significant screening effects. This behavior persists even at temperatures much larger than the QCD phase transition, where on general grounds, one would expect that the confining potential disappears because of Debye screening [15].

This problem was solved recently [16] by carefully disentangling the different time scales in the problem. Taking into account the remnants of early-time

nonpotential physics, the lowest lying spectral peak was found to deviate from a naive Lorentzian shape through skewing. Extracted values for real and imaginary parts based on this functional form result in a potential that is compatible with Debye screening.

In this paper our aim is twofold: first, we wish to ascertain whether fitting of the lowest lying spectral peak indeed suffices to determine the static heavy quark potential, given the spectral function of the Wilson loop or even the gauge fixed Wilson line correlators. Subsequently, it is our goal to better understand the challenges facing a numerical determination of the spectral function by Bayesian analytic continuation. Since in the perturbative approach both the Euclidean correlator and spectrum are known, the outcome of the numerical reconstruction can be readily compared.

In Sec. II we review the basics of the method of Ref. [14] and its improvement introduced in [16], which form the basis of the extraction of the potential from lattice simulations. From calculations of the real-time Wilson loop as well as gauge fixed Wilson line correlators in Sec. III, we determine and investigate the corresponding spectral functions in Sec. IV. While in Sec. V we apply the peak fitting procedure of [16] to the HTL spectra, Sec. VI scrutinizes how well these spectra can be obtained with the maximum entropy method [17] from the HTL Euclidean correlators. Our conclusion in Sec. VII discusses the limitations of the method and points toward further possible improvements.

II. HEAVY QUARK POTENTIAL FROM EUCLIDEAN CORRELATORS

The description of the interactions between a pair of heavy quarks and antiquarks at finite temperature in terms of a quantum mechanical potential $V(r)$ requires the relevant physics to be well separated from the energy scale of pair creation. In particular,

$$\frac{\Lambda_{\text{QCD}}}{m_Q} \ll 1, \quad \frac{T}{m_Q} \ll 1 \quad (1)$$

needs to be fulfilled,¹ which is satisfied exactly in the static limit ($m_Q \rightarrow \infty$). In that case, the propagation amplitude of an infinitely heavy quark pair can be described by a rectangular temporal Wilson loop $W_{\square}(t, r)$, where t, r are its temporal and spatial extent. This real-time quantity is defined as the closed contour integral over the matrix valued gauge field $A^{\mu}(x) = A_a^{\mu}(x)T^a$ along the path of the heavy quarks,

$$W_{\square}(t, r) = \frac{1}{N_c} \mathcal{P} \text{Tr} \left[\exp \left[-ig \oint_{\square} dx^{\mu} A_{\mu}(x) \right] \right]. \quad (2)$$

If the scale hierarchy holds, it is permissible to substitute the field theoretical interactions by an instantaneous

potential, so that $W_{\square}(t, r)$ obeys a Schrödinger-type equation

$$i\partial_t W_{\square}(t, r) = \Phi(t, r) W_{\square}(t, r). \quad (3)$$

At late times, one expects the function $\Phi(t, r)$ to become time independent, so that we may define the heavy quark static potential as

$$V(r) = \lim_{t \rightarrow \infty} \Phi(r, t). \quad (4)$$

Due to the complex weighting factor in Feynman's path integral, we cannot calculate the real-time Wilson loop using lattice QCD Monte Carlo simulations. Instead we have to rely on an analytic continuation of Euclidean time quantities that are accessible by these numerical methods. In order to connect the heavy quark potential $V(r)$ and the Euclidean Wilson loop, one introduces a spectral representation of the real-time quantity,

$$W_{\square}(r, t) = \int d\omega e^{-i\omega t} \rho_{\square}(r, \omega), \quad (5)$$

where the time dependence now resides entirely in the integral kernel. Note that the function $\rho_{\square}(r, \omega)$ is not just a Fourier transform but can be shown to be a positive-definite spectral function [19].² After analytic continuation $t = -i\tau$ one observes that only the integral kernel has changed, whereas the spectral function remains the same,

$$W_{\square}(r, \tau) = \int d\omega e^{-\omega\tau} \rho_{\square}(r, \omega). \quad (6)$$

Using the MEM, a form of Bayesian inference, it is in principle possible, albeit challenging, to invert Eq. (6) and thus to extract the spectral function from $W_{\square}(r, \tau)$. Note that the model-independent method of Refs. [24–26] is not directly applicable, as the Wilson loop is not periodic. However, a similar method could probably be developed from the general results of Refs. [27,28]. Once we are in possession of the spectral function ρ_{\square} we can insert Eq. (5) into Eq. (4), which yields [19]

$$V(r) = \lim_{t \rightarrow \infty} \frac{\int d\omega \omega e^{-i\omega t} \rho_{\square}(r, \omega)}{\int d\omega e^{-i\omega t} \rho_{\square}(r, \omega)}. \quad (7)$$

Direct application of this formula in the case of a numerically reconstructed spectral function is very difficult. It is, however, possible to determine those structures in the spectral function which dominate the integral in the infinite time limit.

If we suppose that the time-independent potential description holds for all times t i.e. $\Phi(t, r) = V(r)$ in Eq. (3), an intuitive connection between spectral features and the

¹See for instance [18] for the discussion of the different limiting cases and their physics.

²It is important to distinguish this r -dependent Wilson loop spectral function from the quarkonium spectral function [20–23] representing the physical quarkonium spectrum.

static potential can be established. In this case Eq. (3) can be solved and the spectral function turns out to be a simple Breit-Wigner peak,

$$\rho(\omega, r) = \frac{\text{Im}[V](r)}{\text{Im}[V](r)^2 + (\text{Re}[V](r) - \omega)^2}, \quad (8)$$

characterized by its peak position $\omega_0(r) = \text{Re}[V](r)$ and width $\Gamma_0(r) = \text{Im}[V](r)$.

In general, the function $\Phi(t, r)$, however, is time dependent at early times, and one expects that a wealth of structures, different from the simple Lorentzian example, exists in the spectrum of the Wilson loop at finite temperature. Note that if the potential description is ultimately applicable, the function $\Phi(r, t)$ will become time

independent at late times, and therefore a corresponding well-defined lowest peak must exist. This part of the spectrum encodes all the relevant information on the potential, and it alone needs to be reconstructed from the Euclidean correlator.

In Ref. [14] it was assumed that the lowest peak is solely described by the late-time behavior of the potential and is not affected by the time dependence of the potential at short times. It was shown in Ref. [16] that this is actually not the case. The short-time dynamics (nonpotential terms, bound state formation) does not just create additional structures at high frequency but also significantly modifies the shape of the low frequency peak. The most general form of this peak, derived in Ref. [16], can be written as

$$\begin{aligned} \rho_{\square}(r, \omega) = & \frac{1}{\pi} e^{\text{Im}[\sigma_{\infty}(r)]} \frac{|\text{Im}[V](r)| \cos[\text{Re}[\sigma_{\infty}(r)] - (\text{Re}[V](r) - \omega) \sin[\text{Re}[\sigma_{\infty}(r)]]}{\text{Im}[V](r)^2 + (\text{Re}[V](r) - \omega)^2} + c_0(r) \\ & + c_1(r) t_{Q\bar{Q}} (\text{Re}[V](r) - \omega) + c_2(r) t_{Q\bar{Q}}^2 (\text{Re}[V](r) - \omega)^2 + \dots \end{aligned} \quad (9)$$

where $\sigma_{\infty}(r) = \int_0^{\infty} dt (\Phi(r, t) - V(r))$ characterizes the early-time physics and $t_{Q\bar{Q}}$ denotes the time during which the integrand $\Phi(r, t) - V(r)$ is nonvanishing. Note that this result can also be obtained from pNRQCD where $\text{Re}[\sigma_{\infty}]$ arises from the phase of the singlet normalization factors $Z_s^{(0)}(r)$ [6].

In order to calculate the potential $V(r)$ from Euclidean correlators we thus need to carry out the following steps:

- (1) Calculate the Wilson loop $W_{\square}(r, \tau)$ at several separation distances r for all possible values along the imaginary time axis $\tau \in [0, \beta]$.
- (2) Use Bayesian inference to extract the most probable spectrum $\rho_{\square}(r, \omega)$ for each value of r .
- (3) Use Eq. (7) to determine the potential $V(r)$
 - (a) by direct Fourier transform of the full $\rho_{\square}(r, \omega)$, which is usually impractical due to the uncertainties introduced by the MEM or
 - (b) by fitting the lowest lying peak with the functional form (9) and analytically carrying out the Fourier transform in Eq. (7).

In the following section we prepare a testing ground for this extraction strategy, based on analytic calculations of the real-time and Euclidean Wilson loop in the HTL resummed perturbative approach. Since the analytic continuation can be performed explicitly in HTL, item 3 of the above list can be tested independently from questions arising from possible inadequacies of the maximum entropy method. The availability of both the spectrum and Euclidean data points furthermore allows us to check the degree of success of the MEM itself in the form of a realistic mock data analysis.

III. CORRELATORS FROM HTL RESUMMED PERTURBATION THEORY

A. Wilson loop

In perturbation theory, the Wilson loop is calculated as an expansion in the coupling:

$$W_{\square}(\tau, r) = W_{\square}^{(0)}(\tau, r) + g^2 W_{\square}^{(2)}(\tau, r) + \mathcal{O}(g^4), \quad (10)$$

starting from $W_{\square}^{(0)} = 1$. The first nontrivial term ($W_{\square}^{(2)}$) contains only a one gluon exchange and is not enough to describe the correct physics for large Euclidean time τ . To improve this situation, we resort to the usual ‘‘exponential’’ resummation [11], noticing that

$$\log(W_{\square}(\tau, r)) = g^2 W_{\square}^{(2)}(\tau, r) + \mathcal{O}(g^4). \quad (11)$$

Thus a better approximation for $W_{\square}(\tau, r)$ is

$$W_{\square}(\tau, r) = \exp(g^2 W_{\square}^{(2)}(\tau, r)) + \mathcal{O}(g^4), \quad (12)$$

as it resums all ‘‘ladder diagrams’’ and contains the correct leading order (g^2) large τ behavior.

1. Leading order term

We now turn to the calculation of $W_{\square}^{(2)}(\tau, r)$, for which we set the r direction along the third spatial axis. In HTL resummed perturbation theory, all diagrams contributing to $W_{\square}^{(2)}(\tau, r)$ have one HTL gluon running between the lines of the Wilson loop [8]:

$$W_{\square}^{(2)} = C_F T \int \frac{d^3 q}{(2\pi)^3} \frac{e^{iq_3 r} + e^{-iq_3 r} - 2}{2} \left\{ \tau^2 \Delta_{00}(0, q) + \sum_{q_0 \neq 0} (2 - e^{iq_0 \tau} - e^{-iq_0 \tau}) \left(\frac{2\Delta_{03}(q_0, q)}{q_0 q_3} + \frac{\Delta_{33}(q_0, q)}{q_3^2} + \frac{\Delta_{00}(q_0, q)}{q_0^2} \right) \right\}. \quad (13)$$

The gluon HTL propagator, written in Euclidean space ($Q^2 = q_i^2 + q_0^2$) and covariant gauge, reads

$$\Delta_{\mu\nu}(Q) = \delta^{ab} \int_Q e^{iQ(x-y)} \left[\frac{P_{\mu\nu}^T(Q)}{Q^2 + \Pi_T(Q)} + \frac{P_{\mu\nu}^L(Q)}{Q^2 + \Pi_L(Q)} + \xi \frac{q_\mu q_\nu}{(Q^2)^2} \right], \quad (14)$$

while the HTL self-energies $\Pi_{E,T}$ are given in Appendix A, and the projectors take the form

$$P_{00}^T(Q) = P_{0i}^T(Q) = P_{i0}^T(Q) = 0, \quad P_{ij}^T(Q) = \delta_{ij} - \frac{q_i q_j}{\mathbf{q}^2}, \quad P_{\mu\nu}^L(Q) = \delta_{\mu\nu} - \frac{q_\mu q_\nu}{Q^2} - P_{\mu\nu}^T(Q). \quad (15)$$

Following Ref. [8], we rewrite the HTL self-energies as spectral functions,

$$\frac{1}{q_0^2 + \mathbf{q}^2 + \Pi_{L,T}(q_0, \mathbf{q})} = \int_{-\infty}^{\infty} \frac{dq^0}{\pi} \frac{\rho_{L,T}(q^0)}{q^0 - iq_0}, \quad (16)$$

so that we can perform the sum over q_0 analytically:

$$W_{\square}^{(2)}(\tau, r) = C_F \int \frac{d^3 \mathbf{q}}{(2\pi)^3} \frac{e^{iq_3 r} + e^{-iq_3 r} - 2}{2} \left\{ \frac{\tau}{\mathbf{q}^2 + \Pi_L(0, \mathbf{q})} + \int_{-\infty}^{\infty} \frac{dq^0}{\pi} n_B(q^0) h(\tau, q^0) \left[\rho_L(q^0, \mathbf{q}) \left(\frac{1}{\mathbf{q}^2} - \frac{1}{(q^0)^2} \right) + \rho_T(q^0, \mathbf{q}) \left(\frac{1}{q_3^2} - \frac{1}{\mathbf{q}^2} \right) \right] \right\}, \quad (17)$$

where we abbreviated the τ dependence of the second term through the function

$$h(\tau, q^0) = 1 + e^{\beta q^0} - e^{\tau q^0} - e^{(\beta - \tau) q^0}. \quad (18)$$

We can write the spatial vector \mathbf{q} in spherical coordinates ($q = |\mathbf{q}|$, θ , ϕ) and $q_3 = q \cos \theta$. In an isotropic plasma, the HTL spectral functions and self-energies depend on q , q^0 only. Integrating over ϕ is trivial and the integral over $c = \cos \theta$ involves

$$\int_{-1}^1 \frac{e^{iqrc} + e^{-iqrc} - 2}{2} dc = 2 \left(\frac{\sin(qr)}{qr} - 1 \right), \quad \int_{-1}^1 \frac{e^{iqrc} + e^{-iqrc} - 2}{2c^2} dc = 2(1 - \cos(qr) - qr \text{Si}(qr)), \quad (19)$$

where Si is the sin integral function. Performing the angular integrals and using $\Pi_E(0, \mathbf{q}) = m_D^2$ gives

$$W_{\square}^{(2)}(\tau, r) = C_F \int_0^{\infty} \frac{dq}{2\pi^2} \tau \frac{q^2}{q^2 + m_D^2} \left(\frac{\sin(qr)}{qr} - 1 \right) + \int_{-\infty}^{\infty} \frac{dq^0}{\pi} \int_0^{\infty} \frac{dq}{2\pi^2} n_B(q^0) h(\tau, q^0) \left\{ \left(\frac{\sin(qr)}{qr} - 1 \right) \left(1 - \frac{q^2}{(q^0)^2} \right) \rho_L(q^0, q) + \left(2 - \frac{\sin(qr)}{qr} - \cos(qr) - qr \text{Si}(qr) \right) \rho_T(q^0, q) \right\}. \quad (20)$$

The first integral in Eq. (20) is linear in τ , whereas the next term is proportional to $h(\tau, q^0)$ and therefore symmetric around $\tau = \beta/2$. We will consider these terms separately in the following:

$$W_{\square}^{(2)}(\tau, r) = W_{\text{lin}}^{(2)}(\tau, r) + W_{\text{sym}}^{(2)}(\tau, r). \quad (21)$$

2. Part linear in τ

The part linear in τ is formally divergent. Using dimensional regularization, the result can be read off from Ref. [8]; the first integral in Eq. (20) hence gives

$$W_{\text{lin}}^{(2)}(\tau, r) = C_F \int_0^{\infty} \frac{dq}{2\pi^2} \tau \frac{q^2}{q^2 + m_D^2} \left(\frac{\sin(qr)}{qr} - 1 \right) = \frac{\tau C_F}{4\pi} \left(\frac{e^{-m_D r}}{r} + m_D \right). \quad (22)$$

In the limit $\tau \rightarrow it \rightarrow i\infty$ this part yields the real part of the potential:

$$\text{Re}[V](r) = g^2 \lim_{t \rightarrow \infty} i \frac{\partial}{\partial t} W_{\text{lin}}^{(2)}(it, r) = -\frac{g^2 C_F}{4\pi} \left(\frac{e^{-m_D r}}{r} + m_D \right). \quad (23)$$

Note that the result is finite (for $r \neq 0$) and the divergence at $r = 0$ reflects the behavior of the Coulomb potential.

On the lattice, this term behaves differently.³ Roughly speaking, the integral is truncated by the lattice cutoff $q < \Lambda$ and thus finite. In this case it is easy to see that it vanishes at $r = 0$, which is expected as a Wilson loop without area is equal to unity. For $r > 0$ it decreases quickly and formally goes to $-\infty$ in the limit of an infinite cutoff.

This behavior cannot be canceled by the other terms in Eq. (20) as they have a different τ dependence. It should not be removed either as it encodes the Coulomb part of the potential that we want to obtain. To make a connection to the lattice, we therefore introduce a UV cutoff, mimicking the finite lattice spacing. In this case, performing the integral over the momentum q from zero to Λ in Eq. (22) gives

$$W_{\text{lin}}^{(2),\Lambda}(\tau, r) = C_F \frac{\tau}{2\pi^2} \left[-\Lambda + m_D \tan^{-1} \left(\frac{\Lambda}{m_D} \right) + \frac{\cosh(m_D r) (\text{Si}(r(im_D - \Lambda)) - \text{Si}(r\Lambda + irm_D))}{2r} - \frac{(\pi - i\text{Ci}(r\Lambda - irm_D)) + i\text{Ci}(irm_D + \Lambda r) \sinh(m_D r)}{2r} \right],$$

where Si, Ci are the sin and cos integral functions. From the UV regularized version of the correlator we get the following potential,

$$\text{Re}[V^\Lambda](r) = g^2 \lim_{t \rightarrow \infty} i \frac{\partial}{\partial t} W_{\text{lin}}^{(2),\Lambda}(it, r), \quad (24)$$

which is plotted in Fig. 7 together with the continuum ($\Lambda \rightarrow \infty$) potential.

3. Symmetric part

We calculate here the symmetric part of the correlator $W_{\text{sym}}^{(2)}(\tau, r)$ corresponding to the second integral in Eq. (20). The functions $\rho_{L,T}(q^0, q)$ receive a contribution from the

cuts of $\Pi_{L,T}$ if $q > |q^0|$. For the opposite case $|q^0| > q$ they vanish except for a δ -function contribution coming from the pole of $\Pi_{L,T}$. In the following we calculate the contribution from the cuts and poles of the transverse and longitudinal self-energies separately,

$$W_{\text{sym}}^{(2)} = W_{\text{cut}}^{(2)} + W_{\text{pole},L}^{(2)} + W_{\text{pole},T}^{(2)}. \quad (25)$$

As before, we introduce a cutoff on the momentum to mimic the effects of the lattice regularization.

Cut contributions.—Using the symmetry $q_0 \leftrightarrow -q_0$, the cuts contribute to the Euclidean Wilson loop as

$$W_{\text{cut}}^{(2)}(\tau, r) = C_F \int_0^\Lambda \frac{dq}{\pi^2} \int_0^q \frac{dq^0}{\pi} n_B(q^0) h(\tau, q^0) \left\{ \left(\frac{\sin(qr)}{qr} - 1 \right) \left(1 - \frac{q^2}{(q^0)^2} \right) \rho_L(q^0, q) + \left(2 - \frac{\sin(qr)}{qr} - \cos(qr) - qr \text{Si}(qr) \right) \rho_T(q^0, q) \right\}, \quad (26)$$

where the integrals should be performed numerically and the functions $\rho_{L,T}$ are given in Appendix A. Note that in Eq. (26), the limit $\Lambda \rightarrow \infty$ is well defined.

Pole contribution from the longitudinal spectral function.—We can write the part of (20) coming from the pole contribution of the electric spectral function as

$$\begin{aligned} W_{\text{pole},L}^{(2)}(\tau, r) &= C_F \int_0^\Lambda \frac{dq}{\pi^2} \int_q^\infty dq^0 n_B(q^0) h(\tau, q^0) \left(\frac{\sin(qr)}{qr} - 1 \right) \left(1 - \frac{q^2}{(q^0)^2} \right) \delta(f_L(q^0)) \\ &= C_F \int_0^\Lambda \frac{dq}{\pi^2} n_B(q_L^0) h(\tau, q_L^0) \frac{1}{|f'_L(q_L^0)|} \left(\frac{\sin(qr)}{qr} - 1 \right) \left(1 - \frac{q^2}{(q_L^0)^2} \right). \end{aligned} \quad (27)$$

Here $q_{L,T}^0$ is the solution of $f_{L,T}(q^0) = 0$, $q^0 > 0$ and the remaining integral is performed numerically. The limit $\Lambda \rightarrow \infty$ also exists in this case (see Appendix B).

Pole contribution from the transverse spectral function.—We proceed in a similar way for the transverse spectral function.

³The difference with dimensional regularization can be traced back to an infinite constant that is removed in the dimensional regularization procedure.

$$W_{\text{pole},T}^{(2)}(\tau, r) = C_F \int_0^\Lambda \frac{dq}{\pi^2} n_B(q_T^0) \frac{h(\tau, q_T^0)}{|f_T'(q_T^0)|} \left(2 - \frac{\sin(qr)}{qr} - \cos(qr) - qr \text{Si}(qr) \right). \quad (28)$$

Here, the limit $\Lambda \rightarrow \infty$ does not exist and the integral in Eq. (28) is linearly divergent (see Appendix B). Note that such divergences were already observed in [29,30], where the Wilson loop of maximal time extent $\tau = \beta$ is shown to diverge at next to leading order. The leading order divergence found in Eq. (28) has yet a different nature and consistently vanishes for $\tau = 0, \beta$. In dimensional regularization, it can be shown (see Appendix C) to match the cusp divergence [31,32], which in this case gives $\frac{C_F g_s^2}{2\pi\epsilon}$ [30].

Here, we are not interested in trying to renormalize the Wilson loop. It is not needed for our purposes as we aim at a comparison with lattice results, which are also not renormalized. It is, however, interesting to note that these cusp divergences do not contribute to the potential and only make the Wilson loop heavily suppressed for $\tau \neq 0, \beta$, hence harder to measure with high accuracy. Removing these divergences in the lattice measurements, without affecting the potential, would be of great help to improve the accuracy of the lattice data. One strategy deployed to this end could be the smearing of gluonic links [33].

4. Imaginary part of the potential

From the symmetric part, we obtain the imaginary part of the potential,

$$i\text{Im}[V]^\Lambda(r) = g^2 \lim_{t \rightarrow \infty} i \frac{\partial}{\partial t} W_{\text{sym}}^{(2),\Lambda}(it, r). \quad (29)$$

As in the end the infinite time limit will be taken, it is sufficient to consider the low frequency part of the q^0 integrals,

$$\begin{aligned} \text{Im}[V]^\Lambda(r) &= g^2 \lim_{t \rightarrow \infty} \frac{\partial}{\partial t} \int_0^\Lambda \frac{dq}{\pi^2} \int_0^q \frac{dq^0}{\pi} n_B(q^0) \\ &\quad \times \frac{q^2}{(q^0)^2} h(it, q^0) \left(\frac{\sin(qr)}{qr} - 1 \right) \rho_L(q^0, q). \end{aligned}$$

Performing the time derivative, using Eq. (A3) and approximating $n_B(q^0) \approx T/q^0$ for small q^0 as well as the identity

$$\lim_{t \rightarrow \infty} \frac{e^{itq^0} - e^{(\beta-it)q^0}}{q^0} = 2\pi i \delta(q^0), \quad (30)$$

we get

$$\text{Im}[V]^\Lambda(r) = -\frac{g^2 C_F}{4\pi} \int_0^\Lambda \left(1 - \frac{\sin(qr)}{qr} \right) \frac{2qm_D^2}{(m_D^2 + q^2)^2} dq,$$

which coincides with the expression obtained in [8,9,11].

5. Numerical evaluation

To make a close connection to actual lattice data with spatial lattice spacing $a = 0.04$ fm, we choose to fix the cutoff in our HTL calculations to

$$\Lambda = \frac{\pi}{a}, \quad (31)$$

which naively corresponds to the largest momentum accessible under this finite resolution. Based on a numerical evaluation of the remaining integrals in Eqs. (21) and (25)–(28), we can generate an arbitrary large number of data points spanning the imaginary time axis, which carry numerical errors of the order of the machine precision only.

Comparing this ideal HTL Euclidean regularized data to actual measurements from a Monte Carlo simulation in Fig. 1, we find a strong qualitative resemblance. Both graphs exhibit three characteristic features. First we find a suppression region at small τ . Second, there is an upward trend at $\tau \approx \beta$. Both are closely linked to the divergences observed in Sec. III A 3. The third feature at intermediate τ , exhibiting nearly exponential behavior, corresponds to those data points that encode the potential. They exhibit

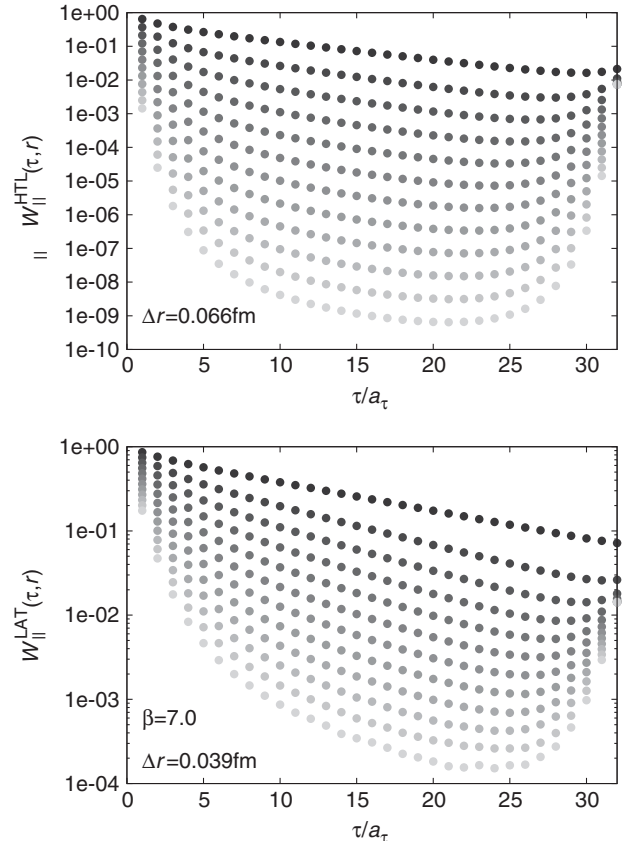


FIG. 1. (Top panel) The Euclidean HTL Wilson loop $W_{\square}^{\text{HTL}}(\tau, r)$ with momentum regularization $\Lambda = 5\pi$ GeV evaluated at $T = 2.33 \times 270$ MeV in steps of $\Delta r = 0.066$ fm (Bottom panel) Quenched lattice QCD Wilson loop from a lattice with $a_s = 0.039$ fm and anisotropy $a_s/a_t = 4$ at $T = 2.33T_C$.

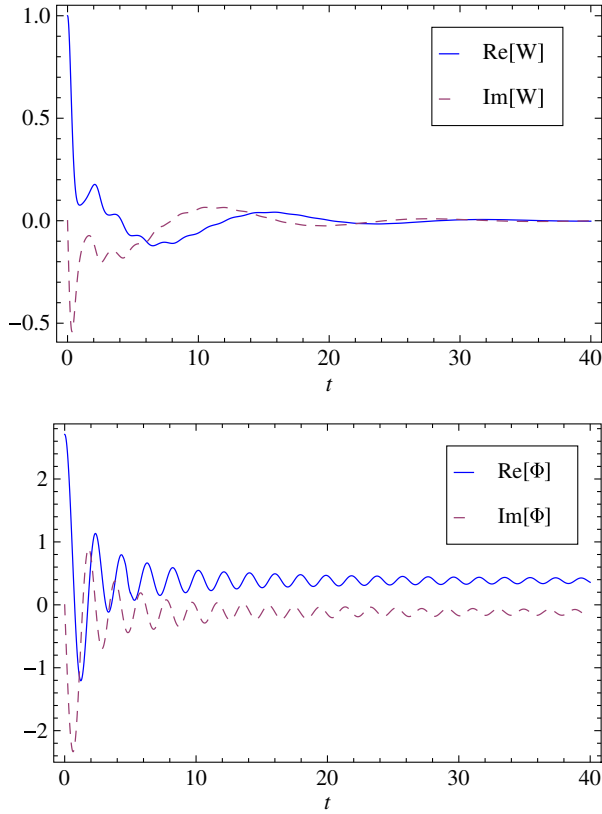


FIG. 2 (color online). (Top panel) The HTL real-time Wilson loop $W_{\square}^{\text{HTL}}(t, r)$ with momentum regularization $\Lambda = \pi \text{ GeV}$ evaluated at $r = 1 \text{ GeV}^{-1}$ and $T = 2.33 \times 270 \text{ MeV}$. (Bottom panel) Time evolution of the quantity $\Phi(t, r)$ obtained from $W_{\square}^{\text{HTL}}(t, r)$ through Eq. (3).

nearly exponential behavior for small separation r , where $\text{Im}[V]$ is also small, but begin to show noticeable curvature for larger separation distances.

After calculating the real-time values $W_{\square}(it, r)$ (see Fig. 2) using a similar numerical evaluation of the integrals in (21) and (25)–(28), it is possible to obtain the function $\Phi(t, r)$. As shown in Fig. 2, we can explicitly observe the approach of $\Phi(t, r)$ to a constant value and thus the emergence of a simple exponential behavior of the Wilson loop. Note that in Fig. 2 we show times $t < 40 \text{ GeV}^{-1}$ where the oscillatory behavior is clearly visible, while a constant value is actually reached for larger t . We refrain from attaching any physical meaning to the length of the swing-in period, as it is dominated by the same cusp divergences that lead to the suppression of the Euclidean Wilson loop data points.

B. Gauge fixed Wilson line correlator

Cyclic Wilson line correlators (i.e. color singlet Polyakov loops) fixed to Coulomb gauge have been extensively studied on the lattice, both for the determination of the zero temperature potential as well as in investigations into the free-energy difference between a medium with and

without heavy quarks inserted (see for instance [34,35]). Due to the absence of spatial Wilson lines connecting the temporal links, these quantities offer a significantly better signal-to-noise ratio than the Wilson loop, especially if the multilevel algorithm [36] is applied.

Besides the technical question of whether the removal of spatial connectors (or e.g. the application of smearing on spatial links) can lead to an improved lattice observable for the extraction of the potential, it is conceptually of interest to understand whether gauge-independent information, such as the potential, can be extracted from a gauge-dependent quantity such as the Wilson line correlators.⁴

We proceed with the determination of the Euclidean time Wilson line correlator analogously to Sec. III A,

$$W_{\parallel}(\tau, r) = 1 + g^2 W_{\parallel}^{(2)}(\tau, r) + \mathcal{O}(g^4). \quad (32)$$

Calculating in leading order HTL resummed perturbation theory we obtain the expression

$$W_{\parallel}^{(2)} = C_F T \int \frac{d^3 q}{(2\pi)^3} \frac{e^{iq_3 r} + e^{-iq_3 r} - 2}{2} \left\{ \tau^2 \Delta_{00}(0, q) + \sum_{q_0 \neq 0} (2 - e^{iq_0 \tau} - e^{-iq_0 \tau}) \frac{\Delta_{00}(q_0, q)}{q_0^2} \right\}, \quad (33)$$

which contains fewer terms than the Wilson loop of (13).

1. Coulomb gauge

In Coulomb gauge, the HTL Euclidean gluon propagator reads

$$\Delta_{\mu\nu}(q_0, q) = \delta^{ab} \int_Q e^{iQ(x-y)} \left[\frac{P_{\mu\nu}^T(Q)}{Q^2 + \Pi_T(Q)} + \frac{Q^2}{q^2} \frac{g_{\mu 0} g_{\nu 0}}{Q^2 + \Pi_L(Q)} \right], \quad (34)$$

where the self-energies $\Pi_{L,T}$ are the same as in covariant gauge (see Appendix A). Inserting the propagator into the expression (33) for the Wilson line correlator gives

$$W_{\parallel}^{(2)} = C_F T \int \frac{d^3 \mathbf{q}}{(2\pi)^3} \frac{e^{iq_3 r} + e^{-iq_3 r} - 2}{2} \times \left\{ \frac{\tau^2}{\mathbf{q}^2 + m_D^2} + \sum_{q_0 \neq 0} \left[\frac{Q^2}{\mathbf{q}^2 q_0^2} \frac{2 - e^{iq_0 \tau} - e^{-iq_0 \tau}}{Q^2 + \Pi_L(Q)} \right] \right\}. \quad (35)$$

We now rewrite the HTL self-energies as spectral functions, use the formulas collected in Appendix A to perform the sum over q_0 and carry out the angular integrations:

⁴The crucial difference to potential models is that we do not investigate the single point $\tau = \beta$, but it is the full Euclidean time dependence of the gauge fixed correlator that is used to reveal the values of the potential.

$$W_{\parallel}^{(2)} = C_F \int q^2 \frac{dq}{2\pi^2} \left[\frac{\sin(qr)}{qr} - 1 \right] \left\{ \frac{\tau}{q^2 + m_D^2} + \int_{-\infty}^{\infty} \frac{dq^0}{\pi} \right. \\ \left. \times \left[\frac{1}{q^2} - \frac{1}{(q^0)^2} \right] \rho_L(q^0) n_B(q^0) h(\tau, q^0) \right\}. \quad (36)$$

We find that the Coulomb gauge Wilson line correlator features a similar structure as the Wilson loop,

$$W_{\parallel}^{(2)}(\tau, r) = W_{\text{lin}}^{(2)}(\tau, r) + \tilde{W}_{\text{sym}}^{(2)}(\tau, r) \quad (37)$$

the symmetric expression however being of much simpler form, depending only on the longitudinal HTL spectral function. At this point we can already anticipate that it is these terms present in both the Wilson loop and Wilson line correlator which contribute to the values of the potential. In particular, the cusp singularity connected to the transverse spectral function identified in section ‘‘Pole contribution from the transverse spectral function’’ is absent from the above expression.

2. Potential from the Wilson line correlator

As in the case of the Wilson loop, a closed expression for the potential can be obtained using

$$V_{\parallel}^{\text{HTL}}(r) = g^2 \lim_{t \rightarrow \infty} i \frac{\partial}{\partial t} W_{\parallel}^{(2)}(it, r) \\ = g^2 \frac{C_F}{2\pi^2} \int dq \left[1 - \frac{\sin(qr)}{qr} \right] \left\{ \frac{q^2}{q^2 + m_D^2} \right. \\ \left. + \int_{-\infty}^{\infty} \frac{dq^0}{\pi} (q^2 - (q^0)^2) \rho_L(q^0) n_B(q^0) \right. \\ \left. \times \frac{e^{itq_0} - e^{(\beta-it)q_0}}{q^0} \right\}. \quad (38)$$

In the infinite time limit one can make use of

$$\lim_{t \rightarrow \infty} \frac{e^{itq_0} - e^{(\beta-it)q_0}}{q^0} = 2\pi i \delta(q^0), \quad (39)$$

which leads us to the same result we encountered for the Wilson loop,

$$V_{\parallel}^{\text{HTL}}(r) = -\frac{g^2 C_F}{4\pi} \left[m_D + \frac{e^{-m_D r}}{r} - iT \phi(m_D r) \right] \quad (40)$$

with the imaginary part given by the integral expression

$$\phi(x) = 2 \int_0^{\infty} dz \frac{z}{(z^2 + 1)^2} \left[1 - \frac{\sin[zx]}{zx} \right]. \quad (41)$$

From a practical standpoint this result is encouraging, as it tells us that (to leading order in HTL) the information content regarding the potential encoded in the Coulomb gauge Wilson line correlator is the same as the one found in the Wilson loop. If such a relation persisted into the non-perturbative realm, the absence of cusp divergences and with it the improved signal-to-noise ratio would make this an ideal observable to reconstruct the potential.

3. Numerical evaluation

As for the Wilson loop we wish to compare the Euclidean HTL correlator to actual values measured in quenched lattice QCD Monte Carlo simulations. While the symmetric term $\tilde{W}_{\text{sym}}^{(2)}$ is finite, the part linear in τ still requires a regularization. We deploy the same momentum space cutoff as introduced in Sec. III A 2 and set its value to $\Lambda = 5\pi$ GeV in the following.

The absence of divergences in the symmetric part of the correlator leads to a significantly different behavior along the imaginary times τ . This can be seen in the top graph in Fig. 3, where we plot the HTL Wilson line correlator and the first five HTL Wilson loops as comparison. The large suppression at early times, as well as the upward trend near $\tau = \beta$, is almost absent. Hence, most of the data points actually carry information on the potential.

Interestingly, in the case of the lattice QCD Wilson line correlator, the upward trend is still visible between the last and second-to-last time step. However, contrary

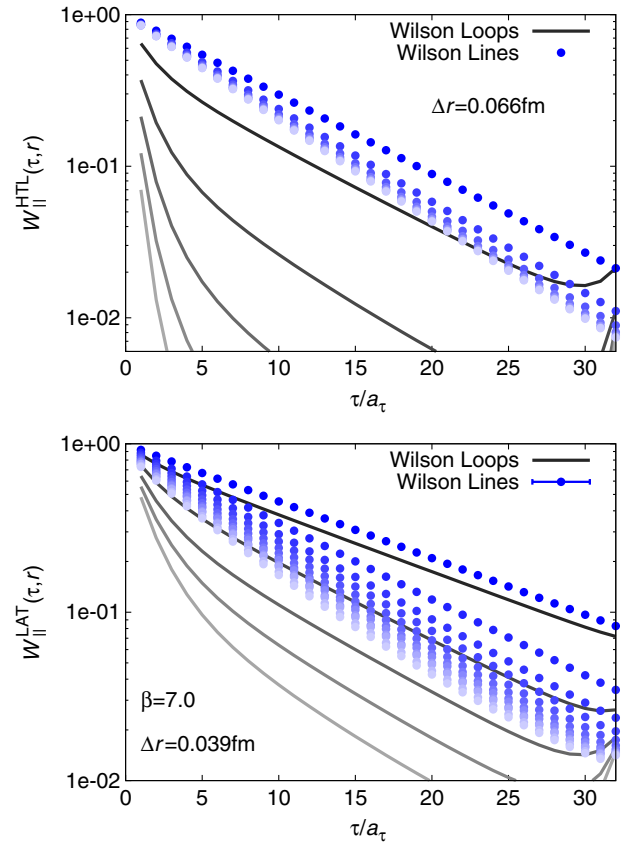


FIG. 3 (color online). (Top panel) The Euclidean time Coulomb gauge HTL Wilson line correlator $W_{\parallel}^{\text{HTL}}(\tau, r)$ with momentum regularization $\Lambda = 5\pi$ GeV evaluated at $T = 2.33 \times 270$ MeV in steps of $\Delta r = 0.066$ fm. (Bottom panel) Quenched lattice QCD Wilson line correlator fixed to Coulomb gauge from a lattice with $a_s = 0.039$ fm and anisotropy $a_s/a_t = 4$ at $T = 2.33T_C$. Note that contrary to the HTL result, the two correlators do not agree at $\tau = \beta$ on the lattice.

to the leading order HTL result, where $W_{\square}^{\text{HTL}}(\beta, r) = W_{\square}^{\text{HTL}}(\beta, r)$, the values of these two different correlators on the lattice do not agree at $\tau = \beta$.

4. Covariant gauge

The Wilson line correlator can be calculated in the covariant gauge as well. The result depends on the gauge parameter ξ and contains additional end-point divergences [37]. These terms, however, do not contribute in the infinite time limit so the obtained potential is again the same as in the Wilson loop case (40).

IV. SPECTRAL FUNCTIONS FROM HTL RESUMMED PERTURBATION THEORY

A. Spectrum of the Wilson loop

The spectral function can be directly calculated from the real-time correlator via a Fourier transform,

$$\begin{aligned} \rho_{\square}(r, \omega) &= \frac{1}{2\pi} \int dt e^{i\omega t} W_{\square}(it, r) \\ &= \frac{1}{2\pi} \int dt e^{i\omega t} e^{g^2 W_{\square}^{(2)}(it, r)} + \mathcal{O}(g^4). \end{aligned} \quad (42)$$

We start by analytically investigating the low frequency behavior of this function, as it allows insight into the spectral structures that encode the physics of the heavy quark potential and will be used in its extraction in Sec. V. To benchmark the MEM extraction of the spectrum from Euclidean correlators it is, however, necessary to compare to the full spectrum, which we will determine from Eq. (42) numerically.

1. Analytical estimate for the low energy part of the spectral function

Starting from Eq. (20), we introduce the momentum cutoff Λ ,

$$\rho_{\square}^{\Lambda}(r, \omega) = \frac{1}{2\pi} \int dt e^{i\omega t} e^{-it \text{Re}[V]^{\Lambda}(r)} e^{\int_{-\infty}^{\infty} \frac{dq^0}{\pi} f_{\square}(q^0)}, \quad (43)$$

where the argument of the second exponential function reads

$$\begin{aligned} f_{\square}(q^0) &= g^2 C_F \int_0^{\Lambda} dq \frac{n_B(q^0)}{2\pi^2} h(it, q^0) \left\{ \left(\frac{\sin(qr)}{qr} - 1 \right) \right. \\ &\quad \times \left(1 - \frac{q^2}{(q^0)^2} \right) \rho_L(q^0, q) \\ &\quad + \left(2 - \frac{\sin(qr)}{qr} - \cos(qr) - qr \text{Si}(qr) \right) \\ &\quad \left. \times \rho_T(q^0, q) \right\}. \end{aligned} \quad (44)$$

For small frequencies, the main contribution to the spectral function (43) comes from small values of q^0 in the above integral. Expanding Eq. (45) around $q^0 = 0$ gives

$$\begin{aligned} f_{\square}(q^0) &= \frac{\text{Im}[V]^{\Lambda}(r)}{2\pi} \left[\frac{2 - e^{itq^0} - e^{-itq^0}}{(q^0)^2} + \frac{e^{itq^0} - e^{-itq^0}}{2q^0} \right] \\ &\quad + \mathcal{O}((q^0)^0). \end{aligned} \quad (45)$$

All terms with negative powers of q^0 are retained in this expression, as they dominate the integral for late times. Note that the imaginary part of the potential appears as an overall factor in the above expression. Within this approximation, the remaining integrals are carried out analytically and we get

$$\begin{aligned} \rho_{\square}^{\Lambda}(r, \omega) &= \frac{k}{2\pi} \left(\frac{e^{\frac{i\text{Im}[V](r)}{2T}}}{|\text{Im}[V](r)| - i(\text{Re}[V](r) - \omega)} \right. \\ &\quad \left. + \frac{e^{-\frac{i\text{Im}[V](r)}{2T}}}{|\text{Im}[V](r)| + i(\text{Re}[V](r) - \omega)} \right) \\ &= \frac{k}{\pi} \frac{|\text{Im}[V](r)| \cos \delta_{\square} - (\text{Re}[V](r) - \omega) \sin \delta_{\square}}{(\text{Im}[V](r))^2 + (\text{Re}[V](r) - \omega)^2}, \end{aligned} \quad (46)$$

with $\delta_{\square} = \frac{\text{Im}[V](r)}{2T}$ and k denoting a normalization constant. From this result, we see that the pole of the spectral function indeed resides at $\omega = \text{Re}[V](r)$ and the width of the peak is closely related to the imaginary part of the potential. The result, however, is not a Lorentzian, but is precisely of the form (9) derived on general grounds in [16]. Note that the phase related to the skewing of the spectral peak is interestingly also given by the imaginary part of the potential,

$$\text{Re}[\sigma_{\infty}] = \delta_{\square} = |\text{Im}[V](r)|/2T. \quad (47)$$

2. Full spectral function

We proceed to calculate the full spectral function by integrating numerically Eq. (42). Applying the discrete Fourier transform to the real-time Wilson loop evaluated on a set of $N_t = 25000$ points separated by a $\Delta t = \frac{1}{50} \frac{1}{\text{GeV}}$, we obtain its values for a wide range of frequencies, partly shown in Fig. 4.

As expected from the minute values of $\text{Im}[V^{\text{HTL}}]$ at small separation distances, the peak one finds is extremely sharp. However, it also becomes clear that the amplitude of the peak is rapidly suppressed as r increases. At the same time, nonpotential contributions related to the divergent terms in the symmetric part of $W^{(2)}(t, r)$ give rise to a huge background structure spanning a wide range of frequencies.

Note that at $\omega \approx 18$ GeV a step in the otherwise smooth spectral function is visible. This is a manifestation of the momentum cutoff we introduced to regularize the formally divergent terms. At the same time, one can observe that the spectrum continues beyond these frequencies, which is a reminder that the cutoff was not imposed on the HTL gluon spectral functions.

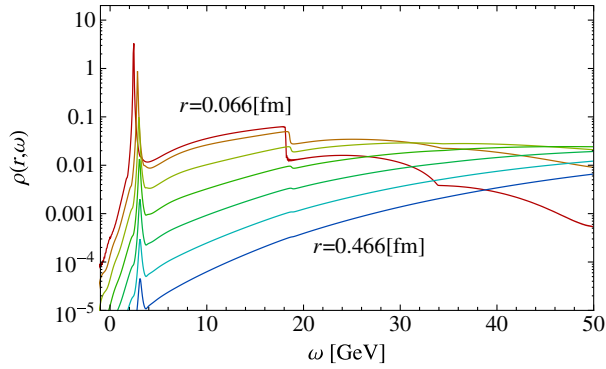


FIG. 4 (color online). The HTL Wilson loop spectral function $\rho_{\square}^{\Lambda}(r, \omega)$ for different spatial separations $\Delta r = 0.066$ fm. Note that the peak is extremely sharp but that its amplitude becomes very small at large r in comparison to the huge background induced mostly by the cusp divergences.

In Sec. V we will use the fitting function (9) to attempt an extraction of the heavy quark potential from the low frequency structures depicted in Fig. 4.

B. Spectrum of the Wilson line correlator in Coulomb gauge

Analogously, we can obtain the spectral function related to the real-time Wilson loop correlator,

$$\begin{aligned} \rho_{\parallel}(r, \omega) &= \frac{1}{2\pi} \int dt e^{i\omega t} W_{\parallel}(it, r) \\ &= \frac{1}{2\pi} \int dt e^{i\omega t} e^{g^2 W_{\parallel}^{(2)}(it, r)} + \mathcal{O}(g^4). \end{aligned} \quad (48)$$

At leading order in the HTL resummed expansion, we again have

$$\rho_{\parallel}^{\Lambda}(r, \omega) = \frac{1}{2\pi} \int dt e^{i\omega t} e^{-it \operatorname{Re}[V]^{\Lambda}(r)} e^{\int_{-\infty}^{\infty} \frac{dq^0}{\pi} f_{\parallel}(q^0)} \quad (49)$$

with

$$\begin{aligned} f_{\parallel}(q^0) &= g^2 C_F \int_0^{\infty} \frac{dq}{2\pi^2} n_B(q^0) h(it, q^0) \left(\frac{\sin(qr)}{qr} - 1 \right) \\ &\quad \times \left(1 - \frac{q^2}{(q^0)^2} \right) \rho_L(q^0, q). \end{aligned} \quad (50)$$

The spectral function can then be calculated analytically close to its peak at small frequency, which yields

$$\rho_{\parallel}^{\Lambda}(r, \omega) = \frac{1}{\pi} \frac{|\operatorname{Im}[V](r)| \cos \delta_{\parallel} - (\operatorname{Re}[V](r) - \omega) \sin \delta_{\parallel}}{(\operatorname{Im}[V](r))^2 + (\operatorname{Re}[V](r) - \omega)^2}.$$

Surprisingly, at leading order in the HTL approximation we find that the skewing characterized by the quantity $\delta_{\parallel} = \frac{|\operatorname{Im}[V](r)|}{2T}$ is exactly the same as for the Wilson loop. Note that the same result can also be obtained in the covariant gauge.

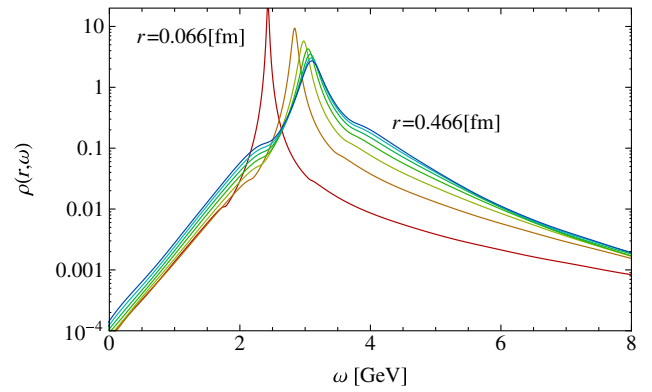


FIG. 5 (color online). The spectral function of the HTL Wilson line correlator in Coulomb gauge $\rho_{\parallel}^{\Lambda}(r, \omega)$ for different spatial separations $\Delta r = 0.066$ fm. While the peak position, width and skewing are exactly as in the Wilson loop case (Fig. 4), the absence of the cusp divergences leads to a significantly reduced background and a much higher amplitude at larger separation distances. Note that the plotting range is much smaller than in Fig. 4.

1. Full spectral function

The full spectral functions for the HTL Wilson line correlator are plotted in Fig. 5. One immediately realizes from a comparison with Fig. 4 that even though the peak position, width and skewing are equal to the Wilson loop case, the Coulomb gauge spectral function looks quite different. The first major difference is that the amplitude of the lowest lying peak depends much less on the separation distance r ; the second is the virtual absence of the background terms populating a large frequency range in the Wilson loop case. Both facts are of course related, since their origin lies in the suppression of the Euclidean Wilson loop correlator induced in the presence of cusp divergences.

V. THE POTENTIAL FROM PERTURBATIVE SPECTRAL FUNCTIONS

Now that we are in possession of the full HTL spectra obtained from both the Wilson loop and the Wilson line correlator in Coulomb gauge, we can test whether the knowledge of the lowest lying spectral features alone suffices to reconstruct the values of the interquark potential in practice. To this end we fit the low ω region of $\rho^{\Lambda}(r, \omega)$ using the functional form (9) and compare the extracted values with the analytically calculated $V^{\text{HTL}}(r)$. We show here the fitting of the Wilson loop spectrum only, since its application to $\rho_{\parallel}^{\Lambda}(r, \omega)$ gives exactly the same results (the potential and the skewing are the same). In Sec. VI, where the numerical reconstruction of the spectra from Euclidean time correlator data is concerned, the differences in e.g. the background contributions will, however, play a major role.

In the following we do not constrain any of the possible fitting parameters; i.e. we allow e.g. $\operatorname{Re}[\sigma_{\infty}]$ and $\operatorname{Im}[V]$ to

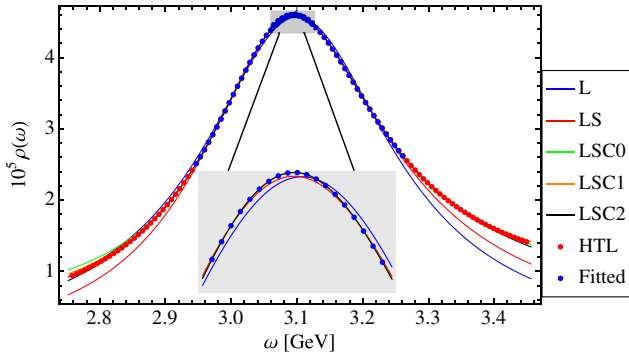


FIG. 6 (color online). Fits to the UV regularized ($\Lambda = 5\pi$ GeV) HTL spectral function $\rho_{\square}^{\Lambda}(r, \omega)$ at $r = 0.49$ fm (right) with a naive Lorentzian (L), a skewed Lorentzian (LS) and a skewed Lorentzian with additional polynomial terms (LSC0, LSC1, LSC2). Note that only the blue points (labeled “Fitted”) are used for the fit and hence only these points enter the determination of the potential.

be determined separately by the fit. To estimate in which cases the use of improved fitting functions becomes necessary, we compare the results from a simple Lorentzian (L) [i.e. $\text{Re}[\sigma_{\infty}] = 0$ and $c_i = 0$ in Eq. (9)], a skewed Lorentzian (LS) [i.e. $c_i = 0$ in Eq. (9)] and the skewed Lorentzian with additional polynomial terms (LSC0, LSC1, LSC2) [i.e. $c_{i>0} = 0$; $c_{i>1} = 0$; $c_{i>2} = 0$ in Eq. (9)].

We find that fitting with L yields reasonable results only at very small separation distances $r < 0.2$ fm, where the width of the peak itself does not exceed 100 MeV. In this distance region, the use of LS improves the fit significantly and actually reproduces the peak shape quite well.

As shown in Fig. 6, at separations of $r = 0.49$ fm the situation is already more involved, as the width of the peaks grows to around 150 MeV and the shape deviates markedly from a naive Lorentzian. Adding the extra degree of freedom of skewing alone does not remedy the situation. Only after including the constant term (LSC0), arising from the early time variation of the function $\Phi(r, t)$, do we find that the spectral shape is reconstructed in an acceptable manner. Including the additional linear (c_1) and quadratic (c_2) coefficients improves the overall agreement with the spectral shape, while the extracted values of the peak position and width are unaffected. This stability against including higher order background terms gives us confidence in the reliability of the fit.

After scrutinizing the goodness of fit, we can turn our attention to the actual values of the potential obtained in this manner. In Fig. 7 the values of the real and imaginary parts of the UV regularized potential $V^{\Lambda}(r)$ are shown in red (solid line) and the values obtained from the Wilson loop spectra fits are overlaid as discrete points. We find that the (LSC) fit successfully reproduces the real part of the potential at least up to the fourth digit. Note that the real part of the regularized potential shows an oscillating

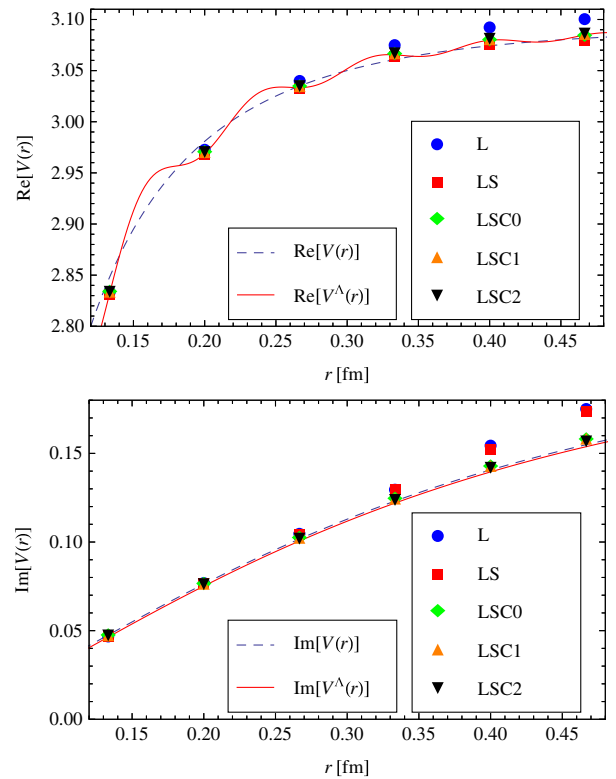


FIG. 7 (color online). Real (top) and imaginary (bottom) parts of the UV regularized ($\Lambda = 5\pi$ GeV) HTL heavy quark potential (red, solid line) at $T = 2.33T_C$, as well as the potential without a cutoff (gray, dashed line). The various symbols denote the extracted values from fits of the HTL Wilson loop spectra based on a Lorentzian (L), skewed Lorentzian (LS) and a skewed Lorentzian with background terms (LSC0, LSC1, LSC2). Note that the simple Lorentzian consistently overestimates the correct values. The determination of the real part suffers only slightly from a worsening of the fit (LSC2 \rightarrow LS), but rough agreement is still visible. On the other hand, a successful extraction of the imaginary part requires at least the presence of the first background term (LSC0), once the width of the spectral peak lies above 150 MeV.

pattern absent in the UV complete $V(r)$, which is retraced by the (LSC) fit. In lattice QCD where both an UV and IR cutoff are present, similar oscillations might arise.

As expected from the fitting of the spectral shapes, the determination of the real and imaginary parts succeeds even for the naive Lorentzian as long as the width is below 100 MeV. We find that the real part is less sensitive to the fitting function, but at larger distances, the Lorentzian overshoots the correct value, preventing us from observing the effect of Debye screening.

The values of the imaginary part show a stronger dependence on the fitting function, and the correct values are only obtained after including the constant term (LSC0). In particular, at large distances $r > 0.3$ fm the simple Lorentzian and even the skewed Lorentzian overestimate the values of the imaginary part.

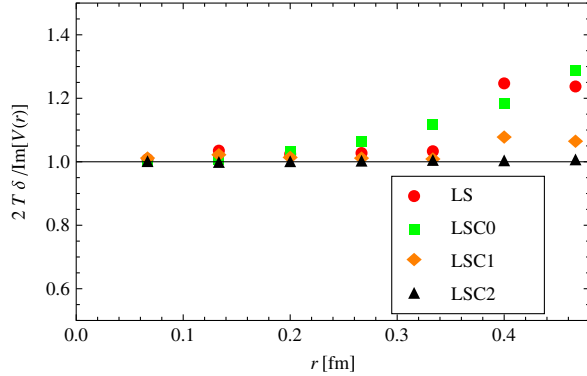


FIG. 8 (color online). Visualization of the connection $\delta_{\square} = \frac{\text{Im}[V]}{2T}$ between the skewing parameter and the imaginary part from the potential peak in the HTL Wilson loop spectrum. For the skewing to be correctly determined, background terms up to quadratic order need to be taken into account.

According to the relation in Eq. (47) it should also be possible to extract the imaginary part of the potential through the skewing parameter δ_{\square} . While for a correct determination of the skewing, a precise fit of the peak shape is necessary, it is indeed possible to use the (LSC) fit to successfully relate the skewing and the imaginary part of the potential as shown Fig. 8.

We conclude, hence, that the extraction of both the real and imaginary parts from Wilson loop spectra succeeds if the improved fitting function Eq. (9) is deployed,⁵ and therefore the knowledge of the shape of the lowest lying peak is sufficient to determine the potential. The results obtained with the (LSC) fit show a negligible deviation from the correct results, and the deviation can be estimated by observing the variation of the fit results when introducing new fit parameters e.g. c_1 . We also find that fitting the lowest peak with a simple Lorentzian leads to an overestimation of both the real and imaginary parts of the potential which contributed to the counterintuitive results of Ref. [14].

VI. MEM ANALYSIS OF THE PERTURBATIVE EUCLIDEAN CORRELATOR

While the extraction of both the real and imaginary parts of the potential from the lowest lying peak structure in $\rho^{\Lambda}(r, \omega)$ has been shown to succeed in the case of known HTL spectra in Sec. V, we now wish to face the numerically challenging aspect of actually reconstructing these spectra from a set of Euclidean-time data points.

⁵We checked that including the next higher order in Eq. (9), i.e. the term linear in frequency with $c_1 \neq 0$, improves the fit at larger $\omega > 3.3$ GeV but does not change the extraction of the parameter values. If we go to higher temperatures, where the width becomes even larger, or if we wish to fit the spectrum over a larger frequency interval around the peak, we will have to include higher terms of the c_i 's.

In the following we will deploy a MEM implementation with extended search space [17] (for technical background see e.g. [38–41]) in an attempt to reconstruct from $N_{\tau} = 32$ ideal imaginary-time data points the most probable spectral function in the Bayesian sense. This number of available measurements along Euclidean time is representative of what we encounter in actual lattice QCD studies of correlation functions. By not adding additional noise and merely attaching artificial error bars to the correlators before feeding them to the MEM, we deliberately choose the best case scenario in which any useful algorithm has to prevail.⁶

A. Wilson loop

To choose appropriate parameters for the MEM we first inspect the Euclidean data points in the top graph of Fig. 2. The strong suppression at small τ as well as the rise at $\tau \approx \beta$ tell us that structures at large positive and negative frequencies contribute to the full spectrum. Thus we decide to discretize ω in an interval $I_{\omega} = [-126, 189]$ GeV by $N_{\omega} = 800$ points using arithmetic with a precision of 384 bits.

The necessity for a large negative value of ω_{\min} , indicated by the data, implies that the N_{τ} basis functions in Bryan's search space do not contain enough variation to capture any peak at positive frequency. Hence we amend the search space by 48 additional basis functions of the full search space, whose oscillations cover the whole range of ω . The Levenberg-Marquardt (LM) algorithm is subsequently used to perform a search for the most probable spectral function within the confines of the above parameters.

Two of the resulting spectra are plotted in Fig. 9. We find that while the presence of the large background is acknowledged by the MEM through several peaks at frequencies $5 \text{ GeV} < \omega < 50 \text{ GeV}$, it is at the same time difficult to obtain a good reconstruction of the lowest lying peak. At $r = 0.066$ at least its position is captured satisfactorily, but the width of the structure remains an order of magnitude too large.

Based on the MEM spectra we can proceed to fit the lowest peak using the fitting function Eq. (9) analogous to the spectra of Sec. V. The results are given in Figs. 10 and 11. The inadequacy of the spectral reconstruction translates here into a consistent overestimation of the values for both the real and imaginary parts of the potential. The shift in the peak position can be understood again from the presence of the large cusp divergence induced background, which together with the limited number of basis functions, pulls the peak towards higher ω in the reconstruction. Similar to observations in

⁶One reasoning behind our choice is that e.g. through the application of the multilevel algorithm it is possible to measure data points with very high accuracy by sacrificing a number of available data points.

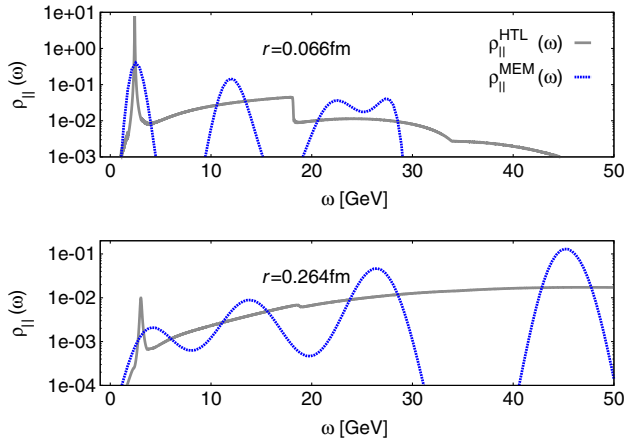


FIG. 9 (color online). MEM reconstructed spectra (dashed, blue line) at $r = 0.066$ fm (top) and $r = 0.264$ fm (bottom) based on $N_\tau = 32$ ideal Euclidean HTL Wilson loop data points at $T = 2.33T_C$. We discretize the frequency interval $I_\omega = [-126, 189]$ GeV by $N_\omega = 800$ points and provide $N_{\text{ext}} = N_\tau + 48$ basis functions for the minimizer to reconstruct $\rho_{\square}^{\text{MEM}}(\omega)$. The exact HTL result at the corresponding distance is given as a gray solid curve. Note that even though the MEM recognizes the presence of the large background terms, it fails to produce a smooth reconstruction. Both the position and shape of the lowest lying peak are rather poorly captured, which we attribute in part to the presence of the large background contribution. The limited number of available degrees of freedom does not suffice to capture both small and large ($\omega > 5$ GeV) structures.

previous lattice QCD based studies, both the real and imaginary parts are of the same order of magnitude.

A few technical comments are in order. Our condition for finding the optimal spectrum in the Bayesian sense relies on a manual stopping criterion for the LM algorithm at relative improvements in the search of $\Delta = 10^{-10}$ to

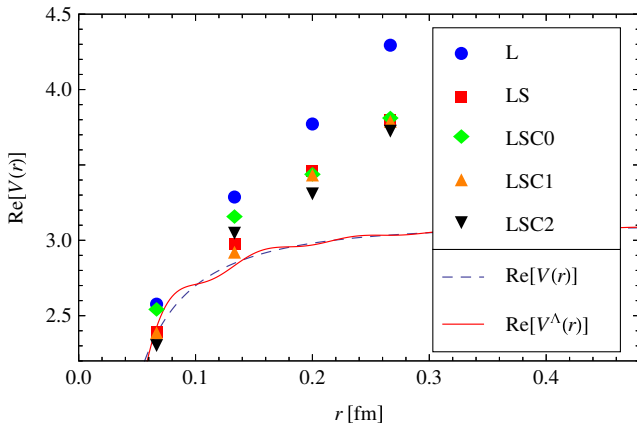


FIG. 10 (color online). The real part of the potential extracted from the MEM reconstructed HTL Wilson loop spectrum at $T = 2.33T_C$. We observe a consistent overestimation of the peak position, which persists even if higher background terms are included in the fitting function (e.g. LSC2). From the results of Sec. V it is apparent that this failure originates in a deficiency of the underlying MEM reconstructed spectra.

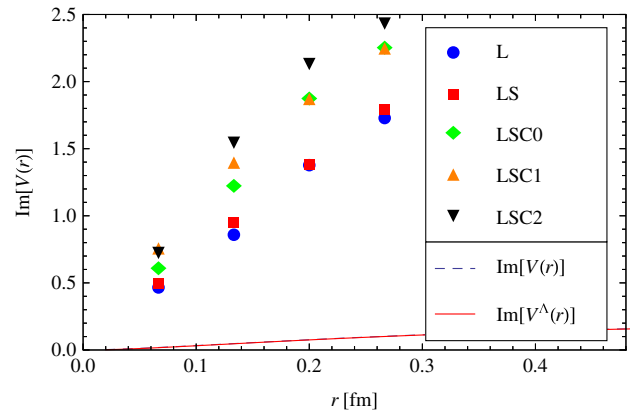


FIG. 11 (color online). The imaginary part of the potential extracted from the MEM reconstructed HTL Wilson loop spectrum at $T = 2.33T_C$. We observe a consistent overestimation of the peak width of more than 1 order of magnitude. Note that including more fitting parameters worsens the estimation of the peak, since the underlying spectra do not actually resemble a skewed Lorentzian.

limit the necessary time for one run to the order of days. This, however, is not yet a true minimum since the values meander around in tiny steps inside the search space without converging to a definite value within machine precision. This fact is sometimes reflected in nonsmooth behavior of the α probability distribution.

Increasing the number of basis functions improves the reconstruction slightly; i.e. the width decreases, but even with $N_{\text{ext}} > 200$ we are not able to reproduce a Lorentzian peak shape including the characteristic tail structures. We furthermore only see marginal improvement in determining the lowest peak, whether the number of data points is increased or the size of the artificially attached error bars is lowered. Since Bayesian inference is based on sound statistical reasoning with a well-defined limit for infinitely many data points and ideal data, these findings lead us to the conclusion that at this point it is not the properties of the supplied data but rather the implementation of the method that prevents us from a successful spectral reconstruction.

It should, however, be noted that a correct reconstruction of the lowest peak is more difficult in the HTL case than what we expect to face on the lattice. Even though remnants of the momentum cutoff Λ are found in the HTL spectrum, the fact that higher frequencies contribute to integrals within the HTL gluon spectral functions, used at intermediate steps of determining $W_{\square}^{\text{HTL}}(\tau, r)$, allows the background to stretch far beyond our choice of $\Lambda = 5\pi$ GeV. The presence of a sharp lattice cutoff would amputate such structures; the corresponding lattice correlator is less suppressed and thus the potential peak more easily reconstructed.

We arrive at a sobering conclusion. Based on the maximum entropy method in its current form, even after

including an extended search space, the reconstruction of the real and imaginary parts from the Wilson loop is extremely challenging. One of the reasons is the presence of the large background structures introduced by the cusp divergences (see Fig. 9), which furthermore suppress the amplitude of the lowest lying peak. All attempts at reconstruction of a sharp peak at small ω are hampered since our limited reservoir of available degrees of freedom is depleted by structures not related to the physics of the potential.

B. Wilson line correlator

The reason to investigate alternative observables such as the Wilson line correlator in Coulomb gauge as a basis for MEM reconstruction is now evident. As we have seen in Sec. III the absence of cusp divergences leads to a dramatically reduced suppression along the Euclidean time axis. The rise at $\tau = \beta$ observed in the Wilson loop is also virtually absent. This bodes well for an application of the standard MEM as the difficulties encountered in the previous subsection were directly connected with the divergence induced background contributions.

We choose to discretize frequencies in an interval $I_\omega = [-63, 126]$ GeV by $N_\omega = 2500$ points. The different choice of frequency range and N_ω compared to the Wilson loop case reflects our expectation that the available degrees of freedom suffice to reconstruct a much more

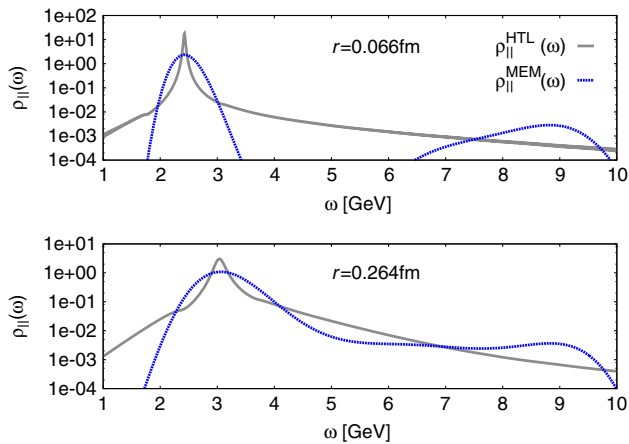


FIG. 12 (color online). MEM reconstructed spectra (dashed, blue line) at $r = 0.066$ fm (top) and $r = 0.264$ fm (bottom) based on $N_\tau = 32$ ideal Euclidean HTL Wilson line correlator data points. We discretize the frequency interval $I_\omega = [-63, 126]$ GeV by $N_\omega = 2500$ points and provide $N_{\text{ext}} = N_\tau + 48$ basis functions for the minimizer to reconstruct $\rho_{\parallel}^{\text{MEM}}(\omega)$. The exact HTL result at the corresponding distance is given as a gray solid curve. Note the absence of large background terms which hampered the reconstruction in the Wilson loop case. While the peak position is captured in a satisfying manner, the width of the reconstructed peaks is almost 2 orders of magnitude too large.

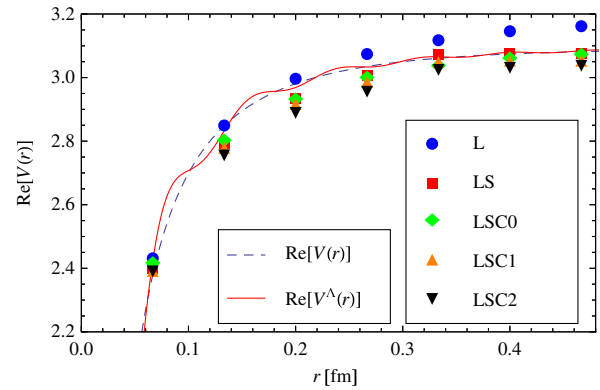


FIG. 13 (color online). The real part of the potential extracted from the MEM reconstructed HTL Wilson line correlator spectrum. After inclusion of skewing, a reasonable agreement with the HTL potential is obtained. Note, however, that the values at larger r did not yet asymptote with respect to the inclusion of higher orders of background terms and tend to underestimate the correct values. The naive Lorentzian fit, on the other hand, leads to values that are too large.

narrow lowest lying peak. The necessity for accommodating a large background is gone.

Figure 12 shows two of the resulting reconstructed spectra which exhibit a much better agreement with the correct HTL result than in the Wilson loop case. Note the factor 5 in the frequency axis compared to Fig. 9. Carrying out a fit with Eq. (9) as in Sec. V allows us to estimate the values of the real and imaginary parts of the potential shown in Figs. 13 and 14.

We observe that at least for the real part a reasonable agreement with the correct $\text{Re}[V^{\text{HTL}}]$ has been obtained, once the skewing is included (LS). What is striking, however, is that the values for different fit functions (LSC0, LSC1, LSC2) do not yet seem to asymptote for larger

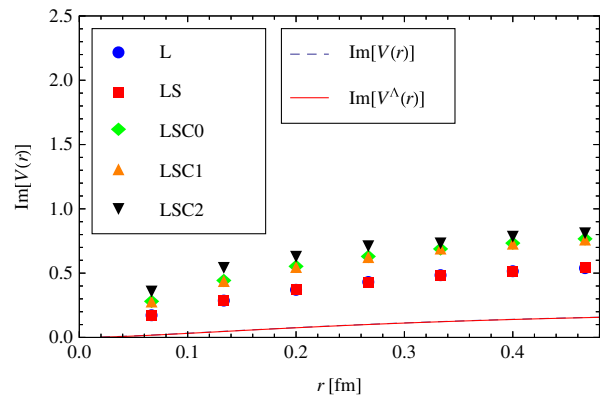


FIG. 14 (color online). The imaginary part of the potential extracted from the MEM reconstructed HTL Wilson line correlator spectrum. Even though a much better resemblance of the reconstructed peaks with the exact HTL spectrum is obtained, we are still a factor 5 away from the actual values of the HTL imaginary part at this temperature.

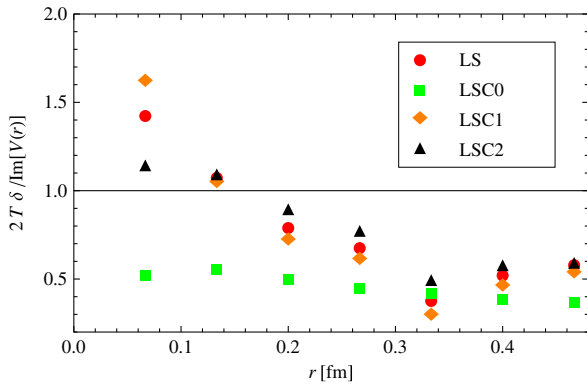


FIG. 15 (color online). Test of the relation $\delta_{\parallel} = \frac{\text{Im}[V]}{2T}$ between the fitted skewing parameter and the imaginary part. We find significant deviations from unity with no clear tendency of improvement. This tells us that at this stage, the reconstructed spectral shapes still do not reliably reproduce a skewed Lorentzian.

separation distances and thus we tend to underestimate the correct values. This behavior is connected to the fact that the shape of the reconstructed spectral peak does not resemble a skewed Lorentzian, as can be seen in Fig. 12.

The estimation of the width of the peak still fares worse compared to the peak position even though the disagreement has been roughly reduced by a factor 3. The absence of the divergences in the Wilson line correlator, and hence the absence of background terms, already leads to a much more narrow reconstructed peak compared to the Wilson loop scenario; it is, however, still not possible to reach the actual width of the exact result.

Since the reconstruction of the peak improved significantly for the Wilson line case, we wish to inspect whether the relation between skewing and peak width is already visible in the MEM spectra. Figure 15 depicts the ratio between the fitting parameter $\delta_{\parallel}^{\text{MEM}}$ and $\text{Im}[V]$ scaled by twice the temperature. The deviations from unity with no clear tendency of improvement tell us that, at this stage, the reconstructed spectral shapes still do not reliably reproduce the skewed Lorentzian functional form actually encoded in the HTL Euclidean data.

If the relation between skewing and the imaginary part should turn out to hold beyond the leading order HTL approximation, it would lend itself to checking the success of the MEM reconstruction. Note that in the Wilson loop case the extracted values of the skewing, besides being completely unstable between different fits, did not show any correlation with the peak width.

Despite the obvious technical shortcomings, which hamper the numerical determination of the potential, our findings are encouraging in that they show how the choice of underlying observable can improve the chances for a successful extraction of the potential.

At least in the leading order HTL approximation, the late real-time physics content is the same whether we are

concerned with the Wilson loop or the Wilson line correlator in Coulomb gauge. The absence of divergences in the latter, however, permits the MEM reconstruction to lie much closer to the correct values.

From the point of view of lattice QCD practitioners, the effects of e.g. the smearing procedure on spatial links in the Wilson loop are connected with modifying physics near the UV cutoff and might therefore also lead to an improved observable with respect to the potential extraction.

VII. CONCLUSIONS AND OUTLOOK

The heavy quark correlator satisfies a Schrödinger equation at late real times, parametrized by a complex potential. It has been proposed that this potential can in principle be extracted from the imaginary-time Wilson loop measured on the lattice [14,16]. The required steps involve an analytic continuation from Euclidean to Minkowski times, usually performed with the help of Bayesian inference and a fitting procedure that connects the position and shape of the lowest lying spectral peak to the real and imaginary parts of the potential, respectively.

Using HTL perturbation theory, we performed a systematic check of the method with the aim to recover the well-known potential of Ref. [8]. At leading order all quantities relevant to the extraction of the potential can be calculated explicitly. After the introduction of a momentum cutoff for large spatial momenta, we were able to determine the full time dependence of both the Wilson loop and Coulomb gauge fixed Wilson line correlator in the Euclidean as well as Minkowskian setting. The discrete Fourier transform is used to calculate the corresponding spectral functions.

We find that the expectations of Ref. [16] are fulfilled, as all spectra contain a well-defined lowest lying peak of skewed Lorentzian form. A major difference between the Wilson loop and Wilson line correlator in Coulomb gauge is the presence of cusp divergences in the former, which translates into large background structures engulfing the potential peak. Nevertheless, the exact same potential is encoded in the two observables at this order in HTL.

A surprising fact is that the skewing parameter, related to the nonpotential physics at early times, is the same for both observables and itself related to the imaginary part of the potential [see Eq. (40)]. It would be very interesting to study whether both of these properties hold beyond the leading order HTL approximation or even on the lattice.

Based on the HTL spectra, we checked whether fitting the functional form derived in [16] succeeds and found that indeed a very accurate determination of the potential is possible from exclusive knowledge of the lowest lying peak. We can hence replace the late real-time limit in (7) by fitting the low frequency realm of the spectrum. We find that the simple Lorentzian consistently overestimates the potential for intermediate and large values of the separation distance r , which offers a partial explanation for the large values observed in previous studies. By including skewing

and higher order background terms from (9), however, we obtain very stable and reliable estimates for $\text{Re}[V]$ and $\text{Im}[V]$.

Our attempts of a standard MEM reconstruction of the spectra from ideal Euclidean time data points revealed several challenges. We found that the large background, induced by the cusp divergences contained in the Wilson loop, makes a reconstruction very difficult. The broad structures not related to the potential absorb a large part of the limited number of degrees of freedom available to the MEM and prevent the potential peak from being captured in a satisfying manner. In addition we are not able to obtain a peak shape that resembles a skewed Lorentzian even after increasing the number of basis functions for the MEM search space or adding additional data points. This leads us to conclude that it is not the properties of the supplied data points but instead the technical implementation of the MEM itself that prevents us from a successful reconstruction.

The situation is significantly improved in the case of the Wilson line correlator in Coulomb gauge, since the cusp divergences and hence the large background contributions in the spectrum are absent. Within the standard MEM it becomes possible to obtain a reasonable estimate of the real part of the potential; the imaginary part is still overestimated by at least a factor of 5. It is still not possible to reconstruct the Lorentzian functional form encoded in the Euclidean correlator, and thus the fits of (9) to both the real and imaginary parts become unstable if too many free parameters (e.g. c_i 's) are included. The favorable UV structure of the Wilson line correlator invites speculation as to whether it can also help us to determine the non-perturbative potential from lattice QCD.

At zero temperature, the potential is extracted from the Coulomb gauge Wilson lines anyway. In this case, it was shown in perturbation theory that at least to NNLO [42] the full Wilson loop matches the Coulomb gauge Wilson lines. The general picture is that if a physical potential description exists at all in the large time limit, the details of the initial condition (how we close the Wilson loop) will not matter.⁷

At nonzero temperature, if the Euclidean correlator is considered, there is no meaning to a large-time limit as $\tau < \beta$. However, if we consider the analytically continued real-time correlator or its spectrum, the infinite-time limit might be considered similarly to the way it is performed at zero temperature. We showed here that the leading order HTL results agree. Hence one might expect, as in the zero temperature case, that the large-time limit of the correlators does not depend on the way we close them at the boundary. Should this assumption hold, then the potential can be extracted from the Wilson line spectrum (or the smeared Wilson loop) as well, although not directly from

the Euclidean data, for which the infinite-time limit does not make sense.

ACKNOWLEDGMENTS

The authors thank N. Brambilla, M. Escobedo, J. Ghiglieri, M. Laine, P. Petreczky, and A. Vario for very helpful discussions and the DFG-Heisenberg group of Y. Schröder at Bielefeld University for generous access to computational resources. This work was partly supported by the Swiss National Science Foundation (SNF) under Grant No. 200021-140234. Y. B. acknowledges partial support by the European Community under the FP7 programme HadronPhysics3.

APPENDIX A: HTL SPECTRAL FUNCTIONS

Inverting the relation (16), we have

$$\rho(q^0) = \frac{\Delta(q_0 \rightarrow -i(q^0 + i0^+)) - \Delta(q_0 \rightarrow -i(q^0 - i0^+))}{2i}, \quad (\text{A1})$$

with $\Delta(q_0) = q_0^2 + \mathbf{q}^2 + \Pi(q_0, \mathbf{q})$. The spectral functions have a pole (gluon for the transverse, plasmon for the longitudinal) in the region $q^0 > q$ and a continuous part in the region $q^0 < q$. They are antisymmetric in q^0 and we restrict the formulas below to $q^0 > 0$. Explicitly, the electric spectral function reads

$$\rho_L(q^0, q) \stackrel{q^0 > q}{=} \pi \delta[f_L(q_0)],$$

$$\rho_L(q^0, q) \stackrel{q > q^0 > 0}{=} \frac{-\frac{\pi m_D^2}{2} \frac{q^0 q}{q^2 - (q^0)^2}}{[q^2 + m_D^2(1 - l(q^0, q))]^2 + [\frac{\pi m_D^2}{2} \frac{q^0}{q}]^2}, \quad (\text{A2})$$

with

$$l(q^0, q) = \frac{q^0}{2q} \ln \left(\frac{q^0 + q}{q - q^0} \right),$$

$$f_L(q_0) = ((q^0)^2 - q^2) \left[1 + \frac{m_D^2}{q^2} (1 - l(q, q^0)) \right].$$

For the transverse spectral function, we have

$$\rho_T(q^0, q) \stackrel{q^0 > q}{=} \pi \delta[f_T(q^0)],$$

$$\rho_T(q^0, q) \stackrel{q > q^0 > 0}{=} \frac{\pi \frac{m_D^2 q^0 q}{4(q^2 - (q^0)^2)}}{[(q^2 + \frac{m_D^2}{2} l(q^0, q)) + \frac{m_D^2 (q^0)^2}{2(q^2 - (q^0)^2)}]^2 + [\frac{\pi m_D^2 q^0}{4q}]^2} \quad (\text{A3})$$

with

$$f_T(q^0) = ((q^0)^2 - q^2) \left[1 + \frac{m_D^2}{2q^2} l(q, q^0) \right] - \frac{(q^0)^2 m_D^2}{2q^3}.$$

⁷Unless, of course, one chooses a divergent gauge, for instance $A_0 = 0$.

APPENDIX B: CONVERGENCE OF THE POLE CONTRIBUTIONS

For the longitudinal spectral function, the solution to the delta function behaves at large q^0 as

$$q_L^0 \simeq \left[1 + 2 \exp\left(-2 \frac{q^2 + m_D^2}{m_D^2}\right) \right].$$

The full integral is then convergent because the factor

$$\left(1 - \frac{q^2}{(q_L^0)^2} \right)$$

is exponentially small.

For the transverse spectral function, at large q , the pole is sitting at

$$q_T^0 \sim \sqrt{q^2 + \frac{m_D^2}{2}} + \mathcal{O}\left(\frac{m_D^2}{g^2} \log \frac{m_D^2}{g^2}\right). \quad (\text{B1})$$

The contribution from the poles is basically given by integrating with respect to q^0 using the δ function,

$$\int dq^0 \delta(f_{L,T}(q^0)) \rightarrow |f'_{L,T}(q^0)|^{-1} \sim 1/q,$$

which gives, in the transverse case, a linear divergence.

APPENDIX C: CUSP DIVERGENCE

We calculate here the divergence coming from the pole of the transverse HTL spectral function (28) in dimensional regularization and show that it matches the cusp divergences.

For $\tau = 0$, β , the function $h(\tau, q_T^0)$ vanishes and hence we have no contribution; note that there are no cusps in these degenerate cases. For $\tau \neq 0$, β , one can decompose the factor

$$n_B(q_T^0)h(\tau, q_T^0) = 1 - \frac{e^{\tau q_T^0} - e^{(\beta-\tau)q_T^0}}{e^{\beta q_T^0} - 1}$$

where the second term leads to a convergent integral.

Using Eq. (B1), the remaining part of the integrand in (28) can also be decomposed as

$$\begin{aligned} & \frac{2 - \frac{\sin(qr)}{qr} - \cos(qr) - qr \text{Si}(qr)}{|f'_T(q_T^0)|} \\ &= \frac{1}{\sqrt{q^2 + m_D^2/2}} - \frac{\pi}{4} r + \text{finite} \end{aligned}$$

where the terms omitted are UV and IR finite. Using dimensional regularization, the linear-divergent term drops and only the τ - and r -independent term survives,

$$W_{\text{pole},T}^{(2)}(\tau, r) = \frac{C_F g^2}{2\pi^2 \epsilon} + \text{finite}. \quad (\text{C1})$$

The cusp multiplicative divergence arising from one angle γ reads [31,32]

$$Z_{\text{cusp}} = 1 + \frac{g^2 C_F}{8\pi^2 \epsilon} (1 + (\pi - \gamma) \cot \gamma).$$

In the Wilson loop case [30] with four angles $\gamma = \pi/2$, we get as a leading order contribution precisely the divergent part of (C1).

-
- [1] T. Matsui and H. Satz, *Phys. Lett. B* **178**, 416 (1986).
 - [2] A. Adare *et al.* (PHENIX Collaboration), *Phys. Rev. Lett.* **98**, 232301 (2007).
 - [3] Z. Tang (STAR Collaboration), *J. Phys. G* **38**, 124107 (2011).
 - [4] S. Chatrchyan *et al.* (CMS Collaboration), *J. High Energy Phys.* **05** (2012) 063.
 - [5] B. Abelev *et al.* (ALICE Collaboration), *Phys. Rev. Lett.* **109**, 072301 (2012).
 - [6] N. Brambilla, A. Pineda, J. Soto, and A. Vairo, *Rev. Mod. Phys.* **77**, 1423 (2005).
 - [7] A. Bazavov, N. Brambilla, X. Garcia i Tormo, P. Petreczky, J. Soto, and A. Vairo, *Phys. Rev. D* **86**, 114031 (2012).
 - [8] M. Laine, O. Philipsen, P. Romatschke, and M. Tassler, *J. High Energy Phys.* **03** (2007) 054.
 - [9] N. Brambilla, J. Ghiglieri, A. Vairo, and P. Petreczky, *Phys. Rev. D* **78**, 014017 (2008).
 - [10] M. A. Escobedo and J. Soto, *Phys. Rev. A* **78**, 032520 (2008).
 - [11] A. Beraudo, J.-P. Blaizot, and C. Ratti, *Nucl. Phys.* **A806**, 312 (2008).
 - [12] N. Brambilla, M. A. Escobedo, J. Ghiglieri, J. Soto, and A. Vairo, *J. High Energy Phys.* **09** (2010) 038.
 - [13] N. Brambilla, M. A. Escobedo, J. Ghiglieri, and A. Vairo, *J. High Energy Phys.* **07** (2011) 096.
 - [14] A. Rothkopf, T. Hatsuda, and S. Sasaki, *Phys. Rev. Lett.* **108**, 162001 (2012).
 - [15] S. Digal, O. Kaczmarek, F. Karsch, and H. Satz, *Eur. Phys. J. C* **43**, 71 (2005).
 - [16] Y. Burnier and A. Rothkopf, *Phys. Rev. D* **86**, 051503 (2012).
 - [17] A. Rothkopf, *J. Comput. Phys.* **238**, 106 (2013).
 - [18] N. Brambilla, M. A. Escobedo, J. Ghiglieri, and A. Vairo, [arXiv:1303.6097](https://arxiv.org/abs/1303.6097).
 - [19] A. Rothkopf, T. Hatsuda, and S. Sasaki, Proc. Sci., LAT2009 (2009) 162.

- [20] Y. Burnier, M. Laine, and M. Vepsalainen, *J. High Energy Phys.* **01** (2008) 043.
- [21] Y. Burnier, M. Laine, and M. Vepsalainen, *J. High Energy Phys.* **02** (2009) 008.
- [22] H.-T. Ding, A. Francis, O. Kaczmarek, F. Karsch, H. Satz *et al.*, [arXiv:1210.0292](https://arxiv.org/abs/1210.0292).
- [23] H.-T. Ding, A. Francis, O. Kaczmarek, F. Karsch, H. Satz, and W. Soeldner, *Phys. Rev. D* **86**, 014509 (2012).
- [24] G. Cuniberti, E. De Micheli, and G. A. Viano, *Commun. Math. Phys.* **216**, 59 (2001).
- [25] Y. Burnier, M. Laine, and L. Mether, *Eur. Phys. J. C* **71**, 1619 (2011).
- [26] Y. Burnier and M. Laine, *Eur. Phys. J. C* **72**, 1902 (2012).
- [27] E. De Micheli and G. A. Viano, *J. Math. Anal. Appl.* **246**, 520 (2000).
- [28] E. De Micheli and G. A. Viano, *J. Math. Anal. Appl.* **234**, 265 (1999).
- [29] Y. Burnier, M. Laine, and M. Vepsalainen, *J. High Energy Phys.* **01** (2010) 054.
- [30] M. Berwein, N. Brambilla, J. Ghiglieri, and A. Vairo, *J. High Energy Phys.* **03** (2013) 069.
- [31] G. Korchemsky and A. Radyushkin, *Nucl. Phys.* **B283**, 342 (1987).
- [32] R. A. Brandt, A. Gocksch, M. Sato, and F. Neri, *Phys. Rev. D* **26**, 3611 (1982).
- [33] A. Bazavov and P. Petreczky, [arXiv:1303.5500](https://arxiv.org/abs/1303.5500).
- [34] Y. Maezawa, T. Umeda, S. Aoki, S. Ejiri, T. Hatsuda, K. Kanaya, and H. Ohno (WHOT-QCD Collaboration), *Prog. Theor. Phys.* **128**, 955 (2012).
- [35] O. Kaczmarek and F. Zantow, *Phys. Rev. D* **71**, 114510 (2005).
- [36] M. Luscher, S. Sint, R. Sommer, P. Weisz, and U. Wolff, *Nucl. Phys.* **B491**, 323 (1997).
- [37] S. Aoyama, *Nucl. Phys.* **B194**, 513 (1982).
- [38] M. Jarrell and J. Gubernatis, *Phys. Rep.* **269**, 133 (1996).
- [39] M. Asakawa, T. Hatsuda, and Y. Nakahara, *Prog. Part. Nucl. Phys.* **46**, 459 (2001).
- [40] A. Jakovac, P. Petreczky, K. Petrov, and A. Velytsky, *Phys. Rev. D* **75**, 014506 (2007).
- [41] D. Nickel, *Ann. Phys. (Amsterdam)* **322**, 1949 (2007).
- [42] Y. Schroder, Ph.D. thesis, Hamburg University, 1999.